Korean J. Chem. Eng., 33(10), 3021-3028 (2016)
DOI: 10.1007/s11814-016-0167-6

pISSN: 0256-1115
eISSN: 1975-7220

Simulation of large biomass pellets in fluidized bed by DEM-CFD

Lingli Zhu, Zhaoping Zhong†, Heng Wang, and Zeyu Wang

Key Laboratory of Energy Thermal Conversion and Control of Ministry of Education,
School of Energy and Environment, Southeast University, Nanjing 210096, China
(*Received 27 January 2016 • accepted 15 June 2016*)

Abstract−An improved numerical model was proposed to solve the problem that the traditional DEM-CFD (Discrete element method-computational fluid dynamics) method was not suitable for the flow simulation of large particles. In the improved model, the large particle was regarded as an agglomerate of many small fictitious spheres. Herein, the drag force between gas and large pellets was assumed as a combined effect of that between gas and fictitious spheres by volume penalty method. Based on the proposed model, the flow of the mixtures of large biomass pellets and quartz sands in fluidized bed was simulated. It shows that the existence of the biomass pellets has a great impact on the flow field. The flow patterns and pressure drops under different working conditions in simulation results have a good agreement with that in experimental results partially, which also tests the proposed model.

Keywords: Multi-phase Systems, Computational Fluid Dynamics, Fluidization, Fluid-particle Dynamics

INTRODUCTION

Due to the energy shortage and stringent emission standards, more and more researchers are trying to discover alternative fuels to substitute for fossil fuel. Biomass pyrolysis technology, which is one of the effective approaches to produce clean liquid fuel with high thermal value, has aroused a worldwide concern. The fluidized bed, comparing with many other reactors, has been widely applied to biomass pyrolysis for high reaction efficiency [1-3]. However, the mixing of fluidizing agents and biomass particles, such as sawdust and rice hull, was not very efficient in the previous researches [4,5]. In which, the layer phenomenon can be easily observed mainly due to the distinct density differences between these two kinds of materials. To solve these problems, compression molding technology is used here to increase the biomass particle density from 600-700 kg/m^3 to 1,300-1,400 kg/m^3. In the present study, the discrete particle simulation of the mixtures consisting of quartz sands and compressed biomass pellets in fluidized bed has been carried out, and authors hope that the successful flow simulation can lay the foundation for pyrolysis or gasification simulation in fluidized bed.

DEM-CFD (Discrete element method - computational fluid dynamics) coupled method, first developed by Tsuji et al. [6], was used to simulate the gas-solid flow in fluidized bed. In the DEM-CFD coupling method, the gas movement is governed by the traditional continuity equation and Navier-Stokes equations, while particle-wall and particle-particle contact force is determined by DEM models [7]. The momentum exchange between gas and solid phase is usually expressed by Ergun [8] and Wen and Yu correlations [9] in mesoscale. With the advantage that the Eulerian approach is able to trace the trajectory of each particle in the simulation process, the DEM-CFD method has been widely used in the simulation of dense gas-solid flow, such as bubbling fluidized bed, spouted bed and rotating fluidized bed [10-12]. In the present study, we applied the DEM-CFD coupling method to simulate the flow of the mixtures consisting of quartz sands and compressed biomass pellets in a fluidized bed. Considering the simulation accuracy, the grid size in DEM-CFD should be not only large enough for the particle size, but also small enough for mesoscopic structures such as bubbles, which limits the application of traditional DEM-CFD coupling method to the simulation of the mixture of large particles and quartz sands (the size of compressed biomass particles is usually larger than 10 mm, while the fluidized agent diameter is less than 1 mm). Inspired by the volume penalty method [13], where the large biomass particle is estimated by assuming that cylinder-shaped particles consisting of small fictitious spheres, the DEM-CFD method is improved and tested in this work.

In this paper, the improved DEM-CFD method for large cylinder-shaped biomass particles was first introduced and then tested by the subsequent numerical simulation of gas flow around a fixed cylinder-shaped particle in a vertical channel. The proposed model was finally implemented in the simulation of the flow of biomass particles and quartz sands.

1. Improved DEM-CFD Model for Large Cylinder-shaped Particles

1-1. Discrete Element Method

The DEM method was proposed by Cundall and Strack, where the collision between particles was modeled by springs, dashpots and sliders. Contacting force in DEM is divided into normal force $\mathbf{f}_{cn}$ and tangential force $\mathbf{f}_{ct}$, which can be calculated by Eqs. (1) and (2) respectively.

$$\mathbf{f}_{cn} = -k_n \mathbf{d}_n - \eta_n \mathbf{v}_n \quad (1)$$

$$\mathbf{f}_{ct} = -k_n \mathbf{d}_t - \eta_t \mathbf{v}_t \quad (2)$$

where, $\mathbf{d}_n$ and $\mathbf{d}_t$ represent the particle displacement in the nor-

†To whom correspondence should be addressed.
E-mail: zzhong@seu.edu.cn

mal direction and tangential direction, respectively, $\mathbf{v}_n$ and $\mathbf{v}_t$ are the particle relative velocity in the normal direction and tangential direction respectively, k is the spring stiffness, and η is the coefficient of viscous dissipation. If $|\mathbf{f}_{ct}|>\mu_f|\mathbf{f}_{cn}|$ is satisfied, $\mathbf{f}_{ct}$ should be calculated by Eq. (3).

$$\mathbf{f}_{ct}=-\mu_f|\mathbf{f}_{cn}|\mathbf{t} \tag{3}$$

where, μ_f is the coefficient of friction. The coefficient of viscous dissipation, η, can be calculated by the following correlations [14]:

$$\eta=2\gamma(\mathrm{mk})^{0.5} \tag{4}$$

$$\gamma=\alpha/(1+\alpha^2)^{0.5} \tag{5}$$

$$\alpha=-(1/\pi)\ln e \tag{6}$$

where, e is the restitution coefficient of spring.

Traditional DEM is not suitable for cylinder-shaped particles, which was discussed above. Hence, the cylinder particle will be assumed as an agglomeration of fictitious spheres in section 1-3.

1-2. CFD Model

Fluid motion is governed by the incompressible continuity and momentum equations.

$$\frac{\partial(\varepsilon)}{\partial t}+\nabla\bullet(\varepsilon\mathbf{u})=0 \tag{7}$$

$$\frac{\partial(\varepsilon\mathbf{u})}{\partial t}+\nabla\bullet(\varepsilon\mathbf{u}\mathbf{u})=-\frac{\varepsilon}{\rho_f}\nabla p+\varepsilon\nu\nabla^2\mathbf{u}+\mathbf{f} \tag{8}$$

where, ε, $\mathbf{u}$ and p represent void fraction, locally averaged gas velocity and gas phase pressure in a computational cell, respectively; ρ_f is the gas density, and ν is gas kinematic viscosity.

Gas-solid interaction force, f, is given by Eq. (9).

$$\mathbf{f}=\frac{\beta}{\rho_f}(\overline{\mathbf{U}}-\mathbf{u}) \tag{9}$$

where, $\overline{\mathbf{U}}$ is the volume-weighted velocity of all solids in a computational cell, which is defined by Eq. (10).

$$\overline{\mathbf{U}}=\frac{N_P V_P\overline{\mathbf{U}}_P+N_{fic}V_{fic}\overline{\mathbf{U}}_{fic}}{N_P V_P+N_{fic}V_{fic}} \tag{10}$$

where, N_p and N_{fic} represent the number of particles and fictitious spheres in a computational cell, respectively, V_p and V_{fic} are the volume of particle and fictitious sphere respectively, $\overline{\mathbf{U}}_P$ and $\overline{\mathbf{U}}_{fic}$ are the average velocity of particles and fictitious spheres in a cell respectively.

The drag coefficient, β, is given by Ergun correlation ($\varepsilon\le0.8$) and Wen & Yu correlation ($\varepsilon>0.8$) [15].

$$\beta=\begin{cases}\dfrac{\mu_f(1-\varepsilon)}{\bar{d}^2\varepsilon}[150(1-\varepsilon)+1.75\widetilde{\mathrm{Re}}] & \varepsilon\le0.8\\ \dfrac{3}{4}C_D\dfrac{\mu_f(1-\varepsilon)}{\bar{d}^2\varepsilon}\varepsilon^{-2.7}\widetilde{\mathrm{Re}} & \varepsilon>0.8\end{cases} \tag{11}$$

$$C_D=\begin{cases}24(1+0.15\widetilde{\mathrm{Re}}^{0.687})/\widetilde{\mathrm{Re}} & \widetilde{\mathrm{Re}}\le1000\\ 0.43 & \widetilde{\mathrm{Re}}>1000\end{cases} \tag{12}$$

where, $\widetilde{\mathrm{Re}}$ is the Reynolds number defined by Eq. (13).

$$\widetilde{\mathrm{Re}}=\frac{|\overline{\mathbf{U}}-\mathbf{u}|\rho_f\varepsilon\bar{d}}{\mu_f} \tag{13}$$

where, $\bar{d}$ is Sauter mean diameter in a computational cell, which can be obtained by Eq. (14).

$$\bar{d}=\frac{1-\varepsilon}{\dfrac{\alpha_p}{d_p}+\dfrac{\alpha_c\alpha_{fic}}{d_{fic}}} \tag{14}$$

where, α_p and α_c represent the volume fraction of particle and cylinder in a computational cell, respectively, and α_{fic} is the volume fraction inside of a cylinder. d_p and d_{fic} are the particle diameter and fictitious sphere diameter, respectively.

The fluid force acting on particle, $\mathbf{f}_p$, and on cylinder, $\mathbf{f}_c$, can be determined by Eqs. (15) and (16).

$$f_p=\frac{\beta V_p(\mathbf{u}-\mathbf{U}_{pi})}{1-\varepsilon}-\nabla p V_P \tag{15}$$

$$f_c=\alpha_{fic}\int_{cylinder}\left(\frac{\beta(\mathbf{u}-\mathbf{U}_{sj})}{1-\varepsilon}-\nabla p\right)dV \tag{16}$$

1-3. Testing of the Improved Model

To test the improved model, the gas flow around a cylinder-shaped particle fixed in the vertical channel is simulated. The geometry of the computational region is shown in Fig. 1(a) (the direction of gas velocity is +z). The grid size is $2.5\times d_{fic}$ in simulation. The arrangement of fictitious particles is shown in Fig. 1(b). The cylinder-shaped biomass particle, both length and diameter of which are 10 mm, is regarded as an aggregation of 2072 fictitious spheres with 0.8 mm (α_{fic}=0.7). C_D is given by Eq. (17).

$$C_D=\frac{2f_c}{\rho_f A_{proj}u_r^2} \tag{17}$$

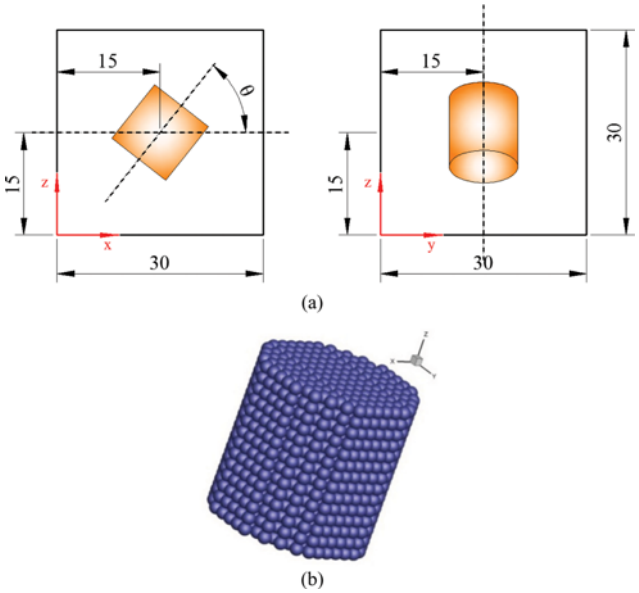

Fig. 1. Geometry of computational region and aggregation of fictitious spheres.

where, u_r is the relative velocity between gas and particle. A_{proj} is the projected surface area of the particle normal to the direction of the relative velocity between the particle and the local gas.

$$A_{proj}=A_0\cos\theta \tag{18}$$

where, A_0 is the maximum cross-sectional area of the cylinder-shaped particle, and θ is the inclination angle, which is also shown in Fig. 1.

C_D values under different Reynolds number and incline angles in simulation are plotted by red line in Fig. 2, while C_D calculated by Eq. (19) [16-18] is depicted by the black line. It is found that C_D value decreases as Reynolds number, Re, increases. As Re<2000, C_D decreases with the increase of Re sharply. However, the decreasing tendency becomes very flat when Re>4000. When Reynolds number is low (Re<2000), C_D value in simulation is less than that calculated by Eq. (19). However, C_D value in simulation becomes much larger when Re>4000.

$$C_D=\frac{24}{Re_P}(1+C_1Re_P^{C_2})+\frac{C_3}{1+(C_4/Re_P)} \tag{19}$$

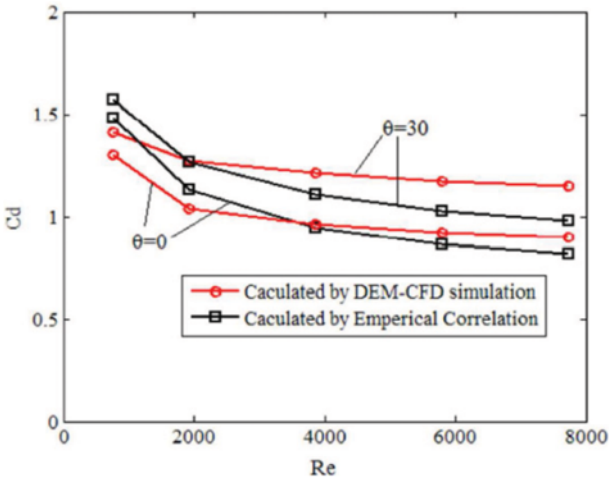

Fig. 2. Comparison of CD value in simulation with that calculated by empirical correlation.

$$\begin{cases} C_1=0.0005\left(\dfrac{\rho_p-\rho_f}{\rho_f}\right)^{1.1687}\varphi^{4.7677}\left(\dfrac{d_a}{d_V}\right)^{6.5032} \\ C_2=0.6813\left(\dfrac{\rho_p-\rho_f}{\rho_f}\right)^{-0.0534}\varphi^{-1.0632}\left(\dfrac{d_a}{d_V}\right)^{-1.5334} \\ C_3=0.6478\left(\dfrac{\rho_p-\rho_f}{\rho_f}\right)^{-0.1328}\varphi^{-3.8035}\left(\dfrac{d_a}{d_V}\right)^{-3.3911} \\ C_4=22.4748\left(\dfrac{\rho_p-\rho_f}{\rho_f}\right)^{-1.764}\varphi^{-1.1738}\left(\dfrac{d_a}{d_V}\right)^{5.1868} \end{cases} \tag{20}$$

2. Simulation and Experimental System

The arrangement of fictitious particles in CFD part is the same as that in the testing part. To form a cylinder in DEM part, 768 spheres with the diameter of 3 mm are used to reduce the time spent in the collision calculation. The quartz sands have an average diameter of 0.8 mm, and function as fluidizing agents. The solution methodology used for DEM-CFD simulation includes the finite volume method (FVM), staggered grid method, semi-implicit method for pressure linked equations (SIMPLE), and the first-order upwind algorithm used for the DEM-CFD iterative process. To reduce the computation time, the computation domain is divided into several sub-domains for parallel computation inspired by the domain decomposition method [19], the scheme of which is shown in Fig. 3. Then computation tasks of different sub-domains are assigned to different CPUs, exchanging the boundary information every calculation step by message passing interface (MPI) command. In the present studies, 12 threads in PC clusters are used for parallel computation at the same time. Other parameters in simulation are shown in Table 1, which are corresponding to the experiment.

The simulated inlet boundary conditions are shown in Fig. 4. The velocity inlet boundary condition is set for the square holes and the no-slip boundary condition is set for the others. The conventional pressure outlet boundary condition is chosen for the outlet boundary. All the mesh size in the direction of x, y, and z is 2 mm. The superficial gas velocity is 1.5 m/s in both the experiment and simulation. So the inlet gas velocity of each discrete hole in the distributor is 19.6 m/s.

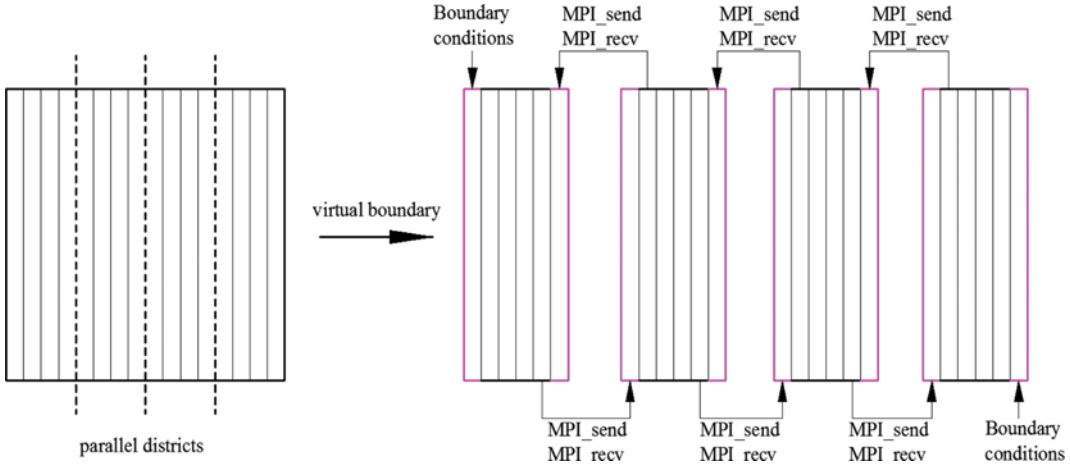

Fig. 3. The schematic of domain decomposition method.

Table 1. System parameters in simulation

Parameter	Unit	Value
Quartz sand diameter	mm	0.8
Quartz sand density	kg/m^3	2700
Quartz sand number		420000
Biomass particle size	mm×mm	10×10
Biomass particle density	kg/m^3	1350
Grid size	mm×mm×mm	2×2×2
Biomass particle number		90
Gas density	kg/m^3	1.205
Gas kinematic viscosity	m^2/s	1.448×10^{-5}
Time step of calculation	s	1.5×10^{-5}
Static bed height	mm	80
Restitution coefficient related to biomass particle		0.43
Restitution coefficient related to sand particle		0.90
Friction coefficient between particles		0.88
Friction coefficient between particle and wall		0.77
Spring stiffness in normal direction	N/m	800
Spring stiffness in tangential direction	N/m	200

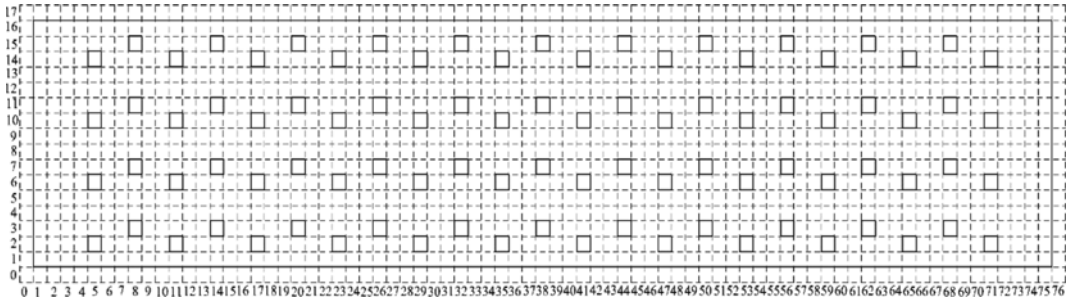

Fig. 4. The schematic of the velocity inlet boundary condition.

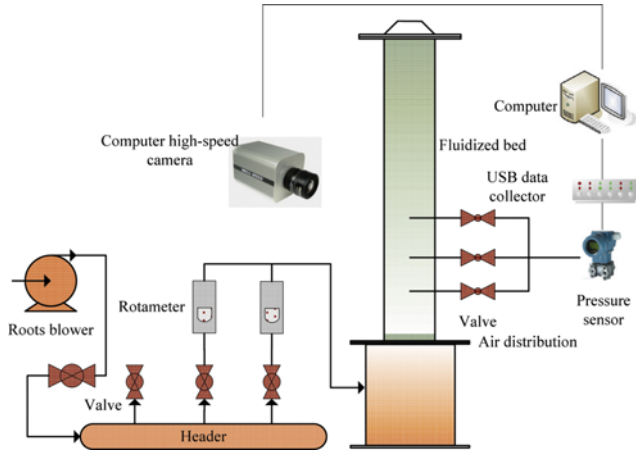

Fig. 5. The schematic of the experimental set-up.

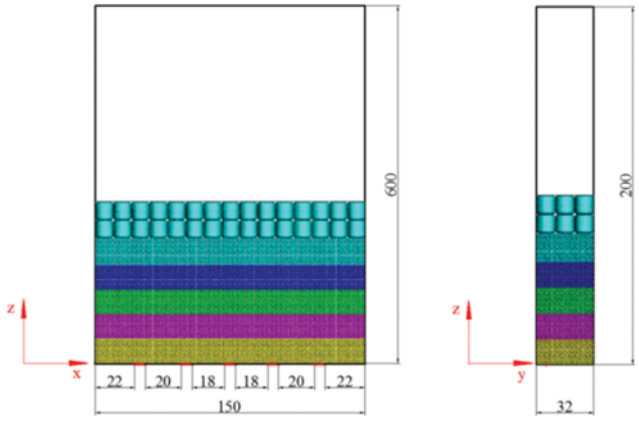

Fig. 6. Geometry of fluidization column.

The fluidization column as depicted in the detailed schematic of the experimental set-up (Fig. 5) is made of Plexiglas, the geometry of which is shown in Fig. 6. Fluidizing air supplied by air compressor is measured by flowmeters to specify the gas velocity over the air distribution on the bottom. The flow regime of the solid phase is shot by CCD camera with the frames per second (FPS) of 30, which is used to compare with the simulation result. To optimize the photo quality, a halogen lamp is used if needed. Pressure sampling system consists of pressure sensor, A/D converter and the terminal computer for collecting the pressure drop signal.

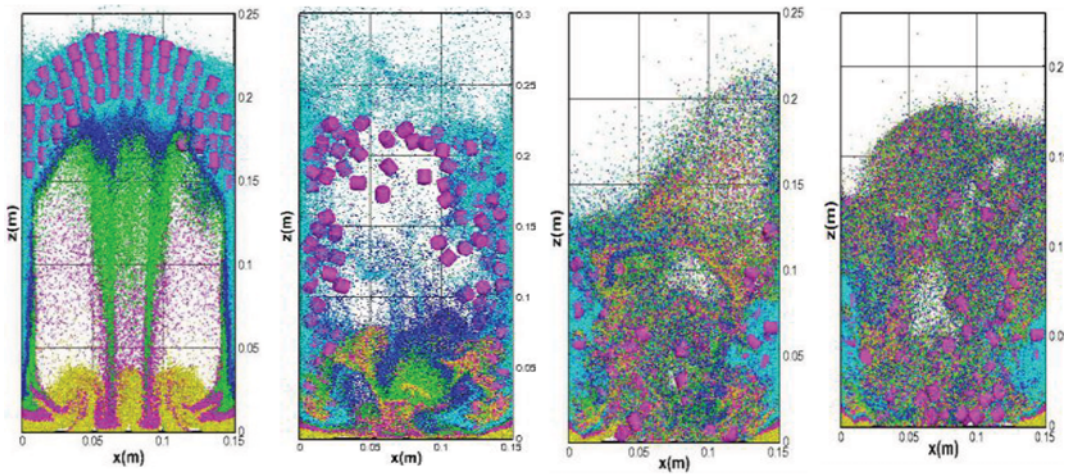

Fig. 7. Snapshots of flow pattern in simulation results (u_f=1.5 m/s, y=10-20 mm).

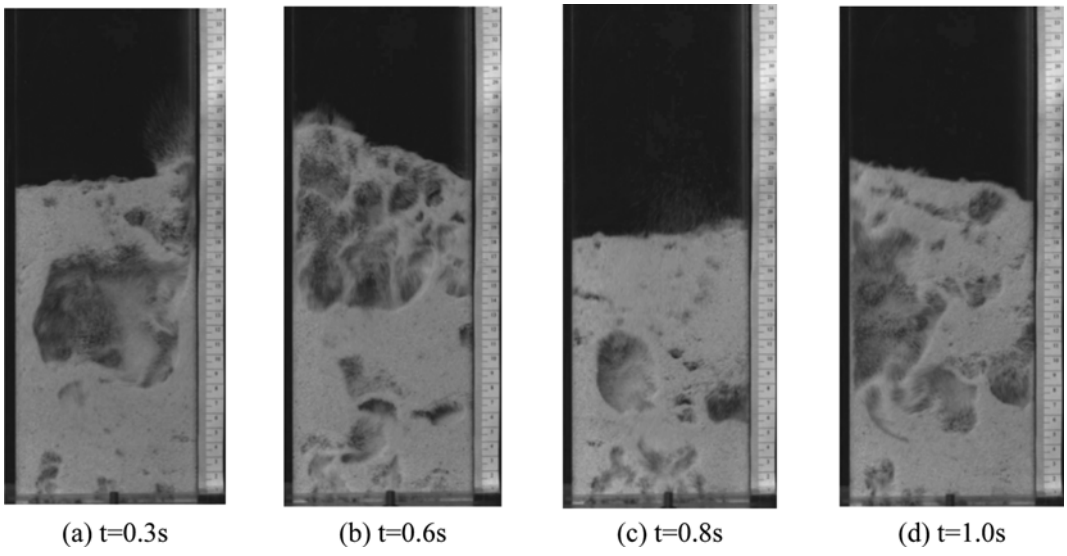

Fig. 8. Snapshots of flow pattern in experimental results (u_f=1.5 m/s).

3. Simulation Results

3-1. Snapshots of the Flow Pattern

Snapshots of the flow patterns in the experiments and simulations are shown in Fig. 7 and Fig. 8, respectively. Although the particle dispersion in the simulation seems a bit different from that of experiment at the beginning stage, which is partly due to the turbulence model unsolved in the simulation, the simulated flow patterns in Fig. 7 are consistent with the visual observations from the physical experiments in Fig. 8 qualitatively. Nonetheless, the simulation still shows good agreement with the experiment, partially in the view of particle motion and mixing progress. From Fig. 7, a typical mixing process is initiated with fine particles regularly arranged under cylinder particles at t=0 s. When the gas flows into the bed from the bottom [Fig. 7(a)], the fine particles are carried up to the top of the bed by the subsequent evolution of bubbles in the central region, which forces the coarse granules to disperse and drop down from both sides at t=0.6 s [Fig. 7(b)]. In addition, the particle mixing progress gradually reaches a more sufficiently mixed stage compared with the initial time for both simulation and experimental result after t=0.8 s.

3-2. Particle and Bubble Motion inside the Fluidized Column

An enlarged picture of particle distribution at the middle-low bed height [Fig. 8(a)] and two enlarged graphics of the velocity vectors [Fig. 8(b), (c)] are presented for a better understanding of the particle transient moving behavior and the causes of the behavior. The areas around the biomass particles have relatively high void fractions, where the minute bubbles easily emerge at the upwind direction. With the combined action of surrounding bubbles and particle conflicts, the biomass particles can change the path of the fine sands around them according to Fig. 9(b) and (c). Moreover, it can also be proven by a similar phenomenon discovered in the experimental pictures as shown in Fig. 8. The main causes of the bubble emergence around the biomass particles are as follows. When the biomass particles are moving upwards, which is shown

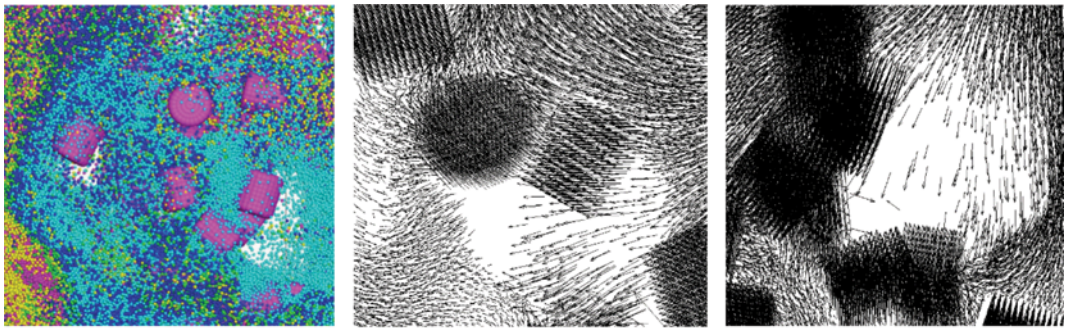

Fig. 9. Enlarged graphic of particle distribution and velocity vectors (Re=800).

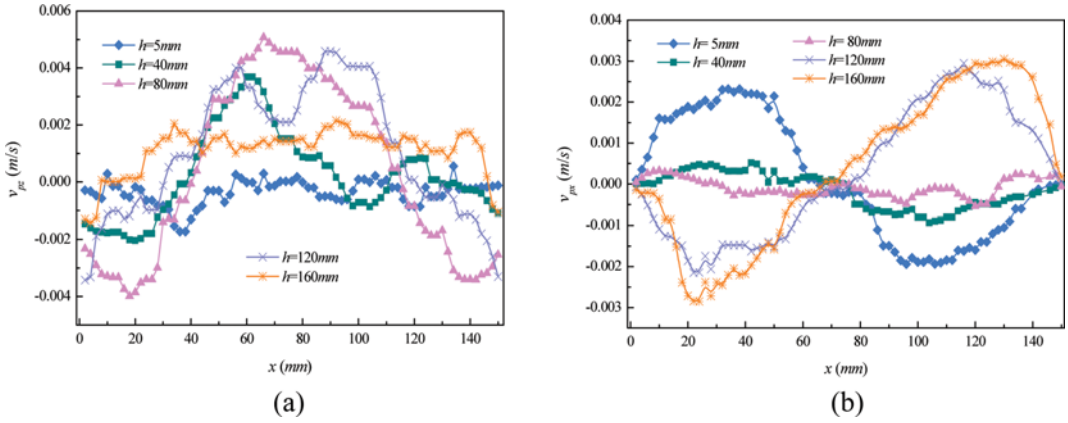

Fig. 10. Time-averaged velocity distribution of the particles (0.9 s-1.5 s).

in Fig. 9(b), the changing of the streamline along the upwind side together with the accelerating of the gas flow along the edges of the biomass particles contributes to the fine particles moving to the edges of biomass particles. In addition, the agglomeration of biomass particles makes the fine particles above the flow field in the stagnating state move at a lower velocity. It results in bubbles emerging, which is shown as Fig. 9(c).

Fig. 10 shows the time-averaged velocity distribution of the particles from 0.9 s to 1.5 s in the simulation results. The time interval used for the time average velocity distribution of particles is 0.6 s. In the section of low bed height the frequent collision of particles puts a high resistance to the moving upwards of particles, causing the velocity to be at a lower level both vertically and horizontally, and the particles moving towards to the central area when h<80

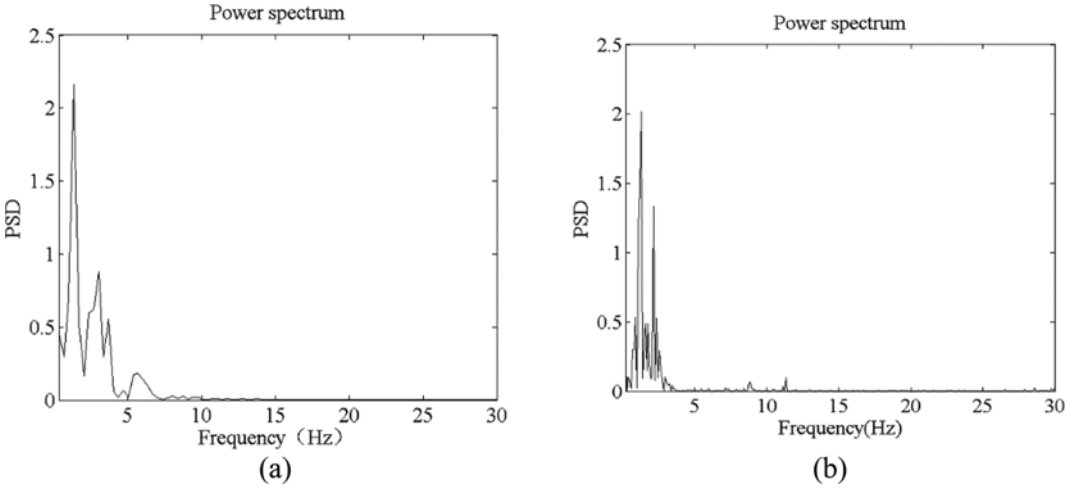

Fig. 11. Power spectrum of pressure fluctuation signal by FFT (u=1.5 m/s).

mm. In the annular section of the column (h=80 mm), particles in the central area have a high vertical velocity while those close to the wall fall down. It is a common phenomenon of the spouted bed. In addition, the particles tend to deviate from the central line to the side when they are blown into the high section of the column (h>120 mm). In general, the particle motion forms an internal circulation inside the fluidized column.

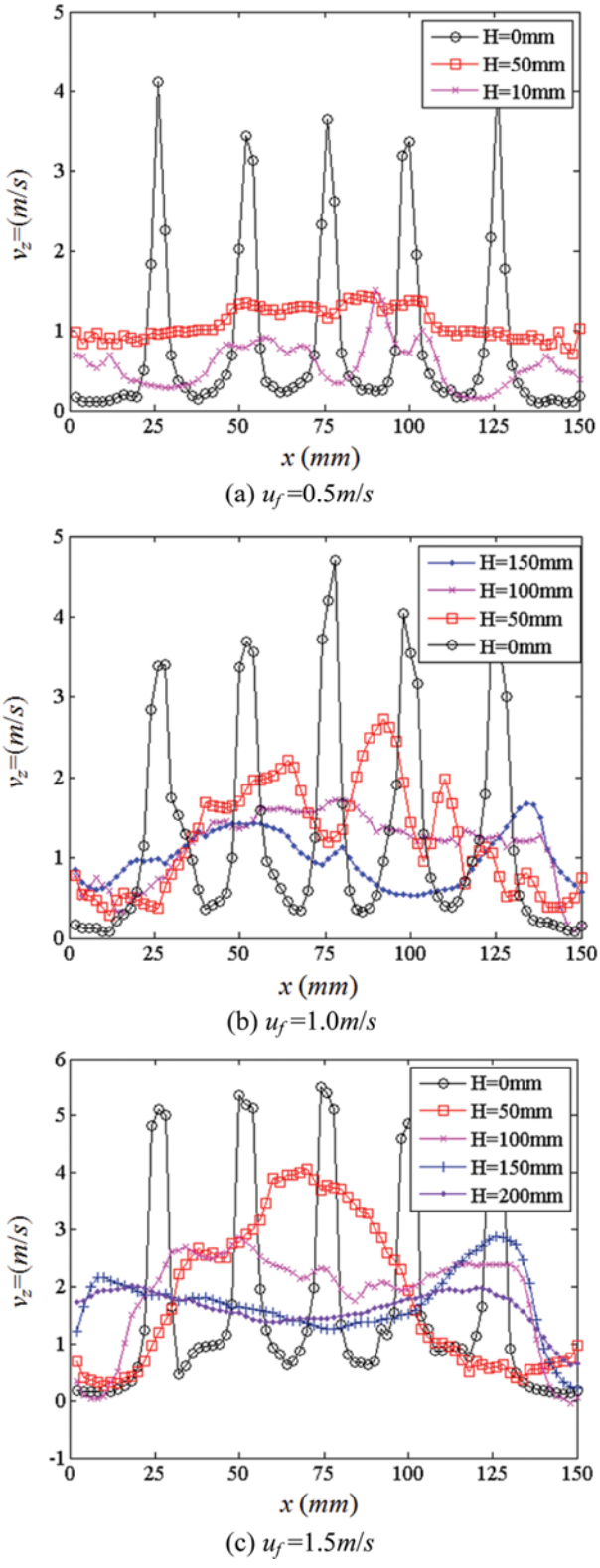

Fig. 12. Gas vertical velocity distribution in the simulation results (0.9 s-1.5 s).

3-3. Pressure Drop and Pressure Fluctuation

The periodic features of time series can be revealed using the spectral analysis through which the frequency of a stochastic system can be detected. The power spectral density (PSD) can be derived from fast Fourier transform (FFT) [20]. Hence, the power spectrum of the pressure signal from both simulated and experimental results by FFT is shown in Fig. 11. Similar to the former part we have discussed, both simulated and experimental results have shown a good consistency with distinct dominant frequency at 1 Hz and 3 Hz, which almost have the same energy for the simulated and experimental results. Considering that the impact of the intrinsic frequency of the fan can be eliminated in the simulation, the power spectrum of the simulated results has a relatively slighter fluctuation compared to the experimental results.

3-4. Gas Velocity Distribution

Fig. 12 shows the vertical velocity distribution of gas phase (0.9 s~1.5 s) in the simulation results. The time interval used for the gas vertical velocity distribution is also 0.6 s. At the bottom of the column, the maximum gas velocity is observed in the central region of jet (x=25, 50, 75, 100, 125 mm). The gas velocity is very low in the boundary region (x=0, 150 mm), which leads to the 'dead zone'. The area of 'dead zone' becomes small as the gas velocity increases. With the height increasing, the gas diffuses from the jet region to the whole column, and the gas velocity in the central zone of the column is larger than that in the boundary region. The central region of jet behavior observed from the simulation is caused by the specific inlet boundary mentioned previously. In the upper region, the velocity distribution along the axial distance becomes uniform.

When the fluidization gas velocity is relatively low, the gas velocity of the whole cross section in the column shows a uniform distribution as depicted in Fig. 12(a). As the gas velocity increases, the vertical velocity reaches a maximum in the central region on the bottom of the bed, while it drops considerably in the surrounding regions with the increasing of the bed height. Furthermore, the vertical gas velocity also shows a uniform distribution in the upper area of the column.

CONCLUSION

The traditional DEM-CFD method is not suitable for the flow simulation of large particles directly. To solve this problem, a model which regards the large cylinder-shaped particle as the agglomerate of many small fictitious spheres was proposed. Based on the proposed model, the flow of biomass pellets and quartz sands in fluidized column was successfully simulated. The particle motion and gas velocity were analyzed. Compared with the experimental results shows the simulation results and experimental results have a good agreement partially.

ACKNOWLEDGEMENTS

This work was sponsored by the National Natural Science Fund

Program of China (51276040 & U1361115).

REFERENCES

1. A. Pattiya, *Bioresour. Technol.*, **102**, 1959 (2011).
2. Q. Xue, D. Dalluge, T. J. Heindel, R. O. Fox and R. C. Brown, *Fuel*, **97**, 757 (2012).
3. W. J. DeSisto, N. Hill, S. H. Beis, S. Mukkamala, J. Joseph, C. Baker, T.-H. Ong, E. A. Stemmler, M. C. Wheeler, B. G. Frederick and A. Heiningen, *Energy Fuels*, **24**, 2642 (2010).
4. R. Li, Z. P. Zhong, B. S. Jin, X. X. Jiang, C. H. Wang and A. J. Zheng, *Can. J. Chem. Eng.*, **90**, 1202 (2012).
5. H. Zhang, R. Xiao, D. Wang, G. He, S. Shao, J. Zhang and Z. Zhong, *Bioresour. Technol.*, **102**, 4258 (2011).
6. Y. Tsuji, T. Kawaguchi and T. Tanaka, *Powder Technol.*, **77**, 79 (1993).
7. P. A. Cundall and O. D. Strack, *Geotechnique*, **29**, 47 (1979).
8. S. Ergun, *Chem. Eng. Progress*, **48**, 89 (1952).
9. C. Y. Wen and Y. H. Yu, *Chem. Eng. Progress*, **62**, 101 (1966).
10. H. Zhou, G. Flamant and D. Gauthier, *Chem. Eng. Sci.*, **59**, 4193 (2004).
11. X. L. Zhao, S. Q. Li, G. Q. Liu, Q. Yao and J. S. Marshall, *Powder Technol.*, **184**, 205 (2008).
12. H. Nakamura and S. Watano, *Powder Technol.*, **171**, 106 (2007).
13. D. Kolomenskiy and K. Schneider, *J. Computational Phys.*, **228**, 5687 (2009).
14. Y. Tsuji, T. Tanaka and T. Ishida, *Powder Technol.*, **71**, 239 (1992).
15. T. Tsuji, K. Higashida, Y. Okuyama and T. Tanaka, *AIChE J.*, **60,** 1606 (2014).
16. B. Maury, *SIAM Journal on Numerical Analysis*, **47**, 1126 (2009).
17. B. Ren, W. Q. Zhong, B. S. Jin, Y. Lu, X. Chen and R. Xiao, *Ind. Eng. Chem. Res.*, **50**, 7593 (2011).
18. B. Ren, W. Q. Zhong, X. F. Jiang, B. S. Jin and Z. L. Yuan. *Can. J. Chem. Eng.*, **92**, 928 (2014).
19. A. Quarteroni and A. Valli, New York, Oxford University Press (1999).
20. J. W. Cooley and J. W. Tukey, *Mathematics of Computation*, **19**, 297 (1965).